On the performance of the M-C (M = Fe, Ru, Os) unit toward gas-phase methane activation

Shihan Li, Xiao-Nan Wu* and Shaodong Zhou*

S. Li and Dr. S. Zhou

College of Chemical and Biological Engineering, Zhejiang Provincial Key Laboratory of Advanced Chemical Engineering Manufacture Technology, Zhejiang University, 310027 Hangzhou (P. R. China);

Zhejiang Provincial Innovation Center of Advanced Chemicals Technology, Institute of Zhejiang University - Quzhou, 324000 Quzhou (P.R. China)

E-mail: szhou@zju.edu.cn

Dr. X.-N. Wu,

School of Biomedical Engineering and Med-X Research Institute, Shanghai Jiao Tong University, Shanghai 200030, P.R. China.

E-mail: wuxiaonan@fudan.edu.cn

Supporting information and the ORCID identification numbers for the authors of this article can be found under: (Wu: 0000-0003-3076-8064; Zhou: 0000-0003-3048-4678)

Supporting Information

Methodology

Experimental details

The experiments were performed in a self-designed, quadrupole-ion trap mass spectrometer (see FigureS1) as described elsewhere.[1, 2] The Metal-carbide cluster ions MC^+ (M = Os and Ru) are generated by pulsed laser(532 nm, Nd:YAG) ablation of a rotating and translating solid target (compressed metal and graphite powder (1:2; volume ratio)) in the presence of Ar carrier gas (99.999%) with a stationary backing pressure of 0.5 MPa. The carrier gas is controlled by pulsed valves. The ions are sent into the quadrupole mass filter through a 5 mm diameter hole of a skimmer, and then the ions are guided into the ion trap (also the reaction cell) through a 5 mm diameter hole of the electric shielding plate and react with CH_4 or CD_4 or $^{13}CH_4$ (reaction time is 10 ms), which is introduced into the reaction cell *via* a leak valve; the experimental uncertainty on the pressure measurement was assumed to be 15% as induced by reading error of the ion gauge (The KJLC 392 type from Kurt J. Lesker Company). Thermalization of the ions is performed in advance by Ar gas that is continuously introduced into the reaction cell; cooling gas pressure of up to 2×10^{-3} Pa and cooling time of 10 ms were used to ensure efficient cooling of the ions. The reaction delay was assumed to be constant. The mass-selection, reaction and mass analysis are all performed in the ion trap.
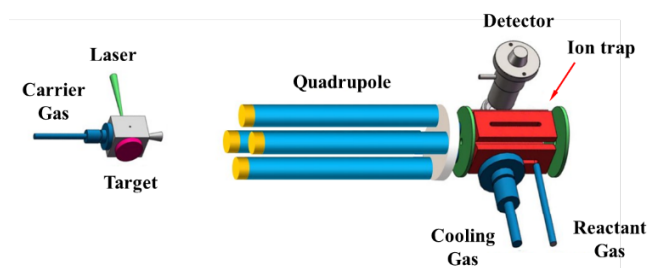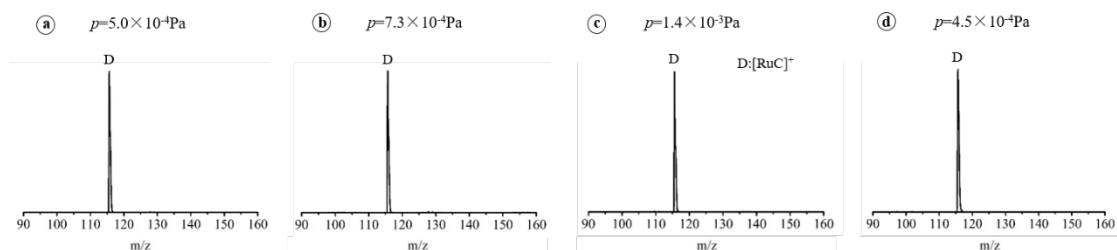

Figure S1 Schematic diagram of the experimental setup.

Figure S2 Mass spectra of the thermal reactions of mass-selected RuC^+(m/z=116) with (a) CH_4, (b) CD_4, (c) $^{13}CH_4$ and (d) Ar.

Computational details

In order to select an appropriate density functional for the $[OsC]^+/CH_4$ reaction system, a benchmark study was performed using the bond dissociation energies (BDEs) of $[Os-H]^+$, $[Os-C]^+$, $[Os-CH]^+$, $[Os-CH_2]^+$, $[Os-CH_3]^+$, $[Ru-H]^+$, $[Ru-C]^+$, $[Ru-CH]^+$, $[Ru-CH_2]^+$ and $[Ru-CH_3]^+$ as criteria (see Table S1 and Table S2). PBE0-D3(BJ) turned out to outperform the others

and was thus used for optimization and frequency analysis. Thus, the structural optimization and frequency analysis were performed at the PBE0-D3(BJ)/def2-TZVP level of theory using the Gaussian 09[3] program. More accurate single-point energies were obtained at the DLPNO-CCSD(T)/def2-TZVPP level of theory. Unrestricted DFT formalisms were used for the open-shell species. Calculations of single-point energies, MECP and the SOC constant were performed with the ORCA 5.0[4] package. Stationary points were optimized without symmetry constraint, and their nature was confirmed by vibrational frequency analysis. Intrinsic reaction coordinate (IRC)[5-7] calculations were also performed to link transition structures with the respective intermediates. Unscaled vibrational frequencies were used to correct the relative energies for zero-point vibrational energy (ZPVE) ontributions. The quasi-restricted orbitals were used for the frontier molecular orbital analysis. Natural bond orbital (NBO)[8-13] calculations were performed to obtain further information on selected stationary points along the reaction paths. The MECP was searched and optimized on the PES using the Surf Cross Opt strategy in ORCA. The analysis of the spin-orbit coupling (SOC) constant at the minimum energy crossing point (MECP) are at the PBE0-D3(BJ)/def2-TZVP level. The Molecular polarity index and Multi-center bond order analysis were generated using Multifwn[14] program.

Figure S3 The detailed potential energy profiles of the reaction of $[OsC]^+$ with CH_4.
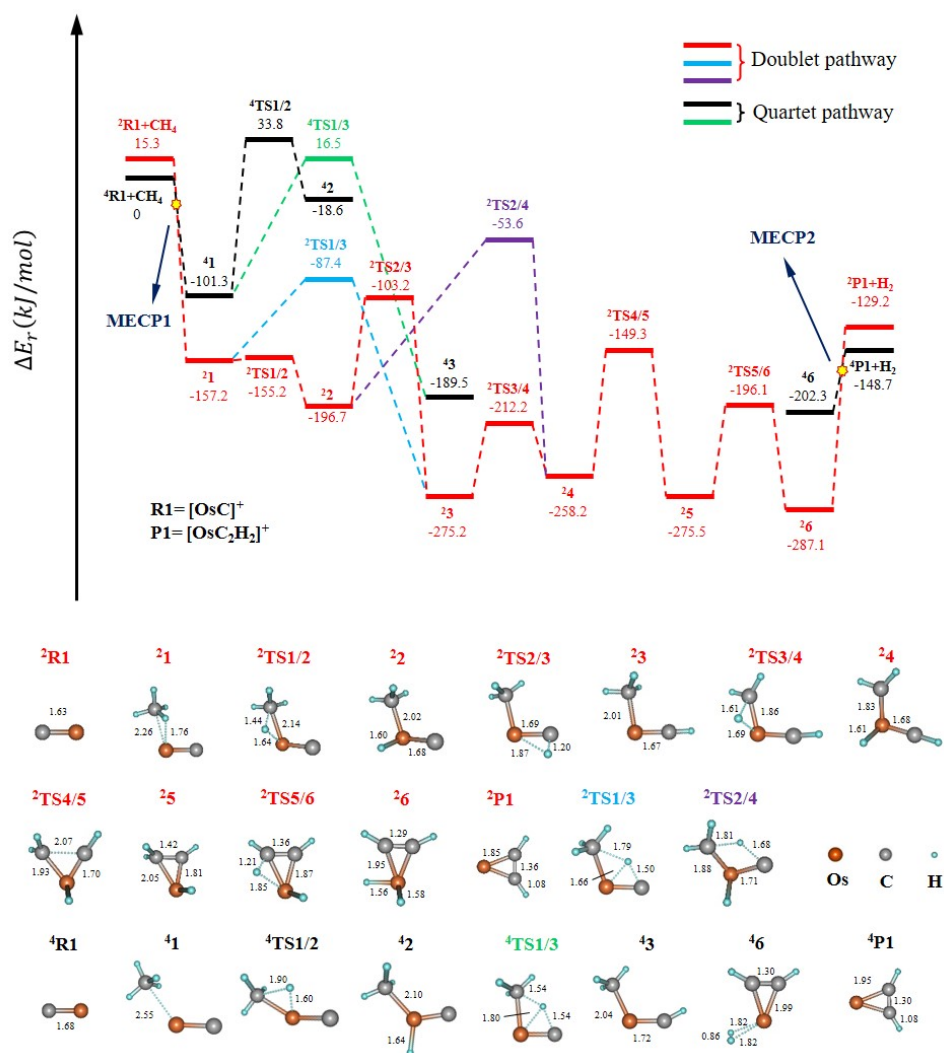
The reaction processes of $[OsC]^+$ with CH_4 are shown in Figure S3. A possible process from intermediate $^2\mathbf{2}$ to intermediate $^2\mathbf{4}$ is supplemented by the transfer of the hydrogen atom from the methyl group to the carbon atom. Obviously, this process is likewise not thermodynamically optimal due to its high energy of intermediate $^2\mathbf{TS2/4}$. In addition, $^4[OsC]^+$ is unable to cross the activation energy barrier of the initial C-H bond to activate methane, either by a three-center activation ($^4\mathbf{1} \rightarrow {}^4\mathbf{TS1/2} \rightarrow {}^4\mathbf{2}$) or a four-center activation process ($^4\mathbf{1} \rightarrow {}^4\mathbf{TS1/3} \rightarrow {}^4\mathbf{3}$). Therefore, $^4[OsC]^+$ has no ability to activate methane.
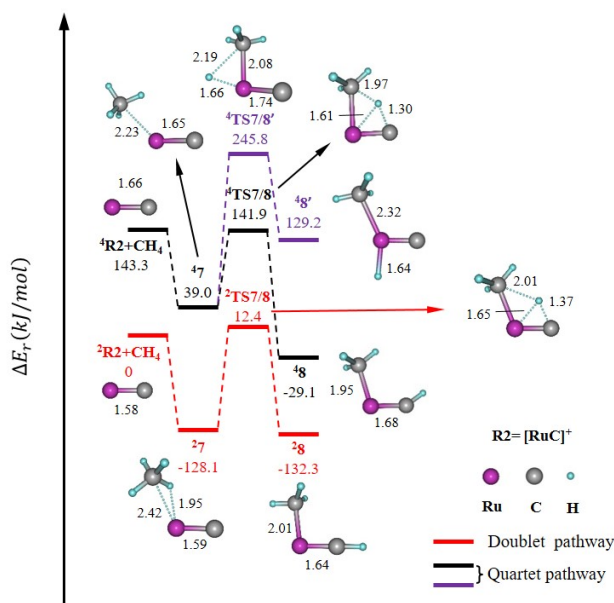

Figure S4 The detailed potential energy profiles of the reaction of $[RuC]^+$ with CH_4.

The reaction processes of $[RuC]^+$ with CH_4 are shown in Figure S4. From this pathway, neither $^2[RuC]^+$ with the lowest energy nor $^4[RuC]^+$ with the sub-lowest energy crosses the activation energy barrier of the initial C-H bond to activate methane. Thus, the $[RuC]^+$ is incapable of activating methane.

Figure S5 The detailed potential energy profiles of the reaction of $[FeC]^+$ with CH_4.

The reaction processes of $[FeC]^+$ with CH_4 are shown in Figure S5. From this pathway, neither $^2[FeC]^+$ with the lowest energy nor $^4[FeC]^+$ with the sub-lowest energy crosses the activation energy barrier of the initial C-H bond to activate methane. Thus, the $[FeC]^+$ is incapable of activating methane.
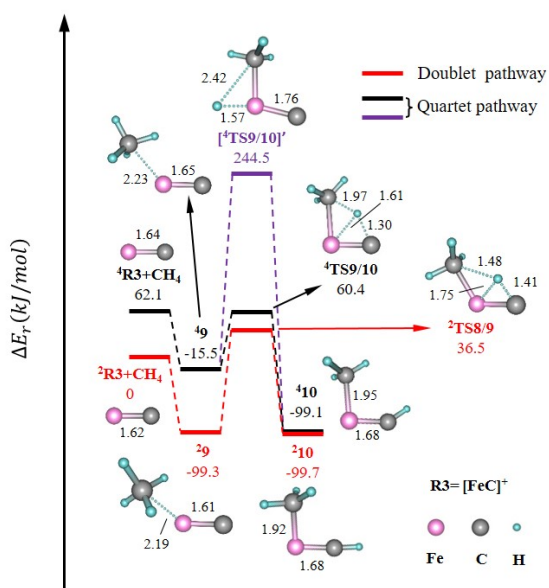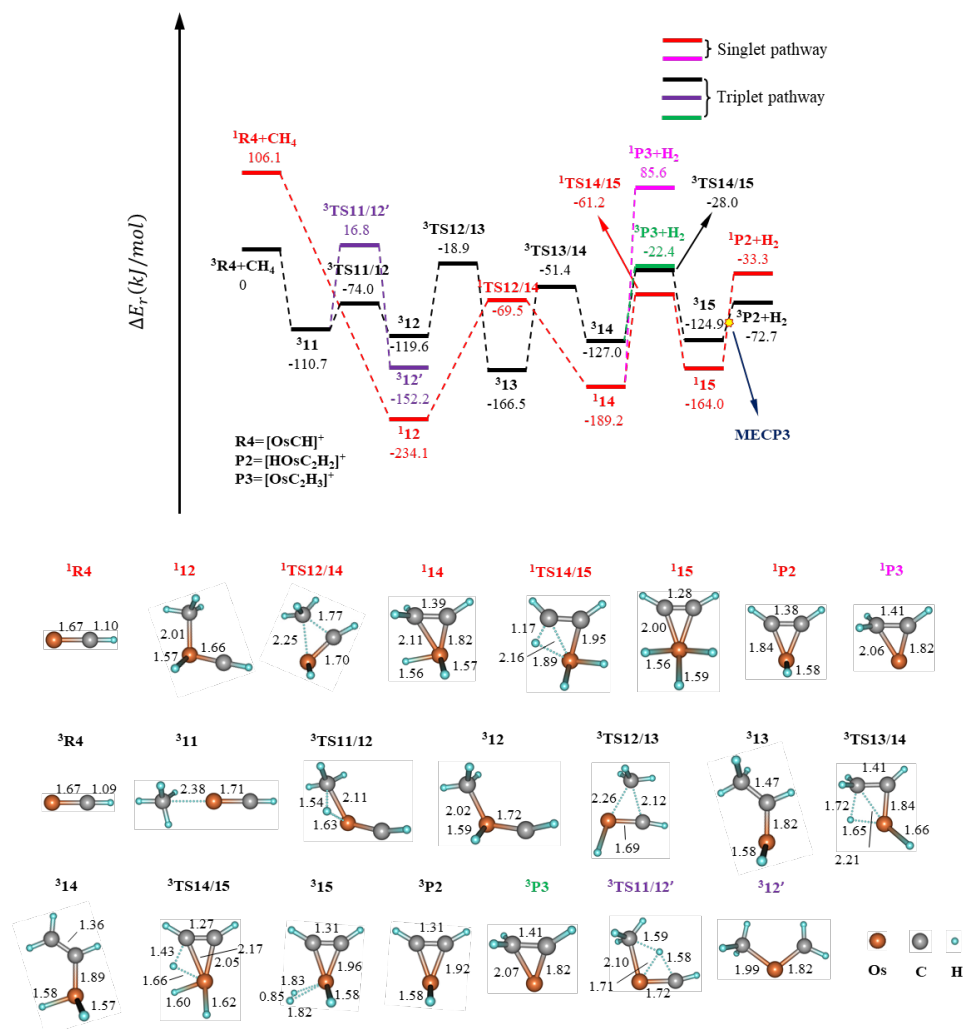

Figure S6 The detailed potential energy profiles of the reaction of $[OsCH]^+$ with CH_4.

The reaction processes of $[OsCH]^+$ with CH_4 are shown in Figure S6. The reaction of $[OsCH]^+$ with CH_4 is carried out in the singlet pathway. Similar to the reaction of $[OsC]^+$ with CH_4, the Os atom is inserted directly between the H_3C-H bond ($^1R4 \rightarrow ^112$). Next, the CH_3 moiety and the hydrogen atom from CH_3 moiety are transferred simultaneously to form C-C, Os-C and Os-H bonds ($^112 \rightarrow ^114$). This is followed by a third transfer of hydrogen from the so-formed methylene to Os ($^113 \rightarrow ^114$), and eventually molecular hydrogen can be eliminated from the complex ($^114 \rightarrow ^3P2$). Here, another spin flip may precede at **MECP3** to eventually afford $^3P2$, as the latter is energetically more stable than its singlet electromer.

However, the reaction pathways for the $^3[OsCH]^+/CH_4$ are diverse. There are two pathways: the insertion into H_3C-H bond by Os atom and four-center activation of CH_4 by inserting OsC unity into H_3C-H bond, and the latter is incapable due to the high energy of intermediate $^3TS11/12'$. Furthermore, the subsequent reaction of $^3[OsCH]^+/CH_4$ is similar to the singlet state, except that the CH_3 group and the hydrogen atom on it are transferred sequentially.

It is noteworthy that the products of hydrogen elimination in both the singlet and triplet states tend to be the more stable $[HOsC_2H_2]^+$ (**P2**) rather than $[OsC_2H_3]^+$ (**P3**) in thermodynamics.

Figure S7 The detailed potential energy profiles of the reaction of $[RuCH]^+$ with CH_4.

The reaction processes of $[RuCH]^+$ with CH_4 are shown in Figure S7. From the pathway, a surface crossing from the triplet state to the singlet state surface (**MECP4**) must occur to form the intermediate **^{1}TS16/17** during the insertion of Ru atom into H_3C-H bond. The reaction then proceeds with the transfer of the so-formed methyl group from Ru atom to CH moiety (^{1}**17→** ^{1}**18**) to form the η^1-CH_3CH ligand. Next, with two more transfers of hydrogen atom from the CH_3 group to the Ru atom (^{1}**18→**^{1}**19→**^{1}**20**), the intermediate **^{1}20** containing three Ru-H bonds is formed. Finally, with the elimination of hydrogen, the product of three hydrogen atoms evenly distributed at Ru and C atoms is produced. Consistent with $[OsCH]^+$, the dehydrogenation product of $[RuCH]^+$ with methane is is thermodynamically optimal for $[HRuC_2H_2]^+$ (^{1}**P4**) rather than $[RuC_2H_3]^+$ (^{1}**P5**) due to the lower energy of the former.
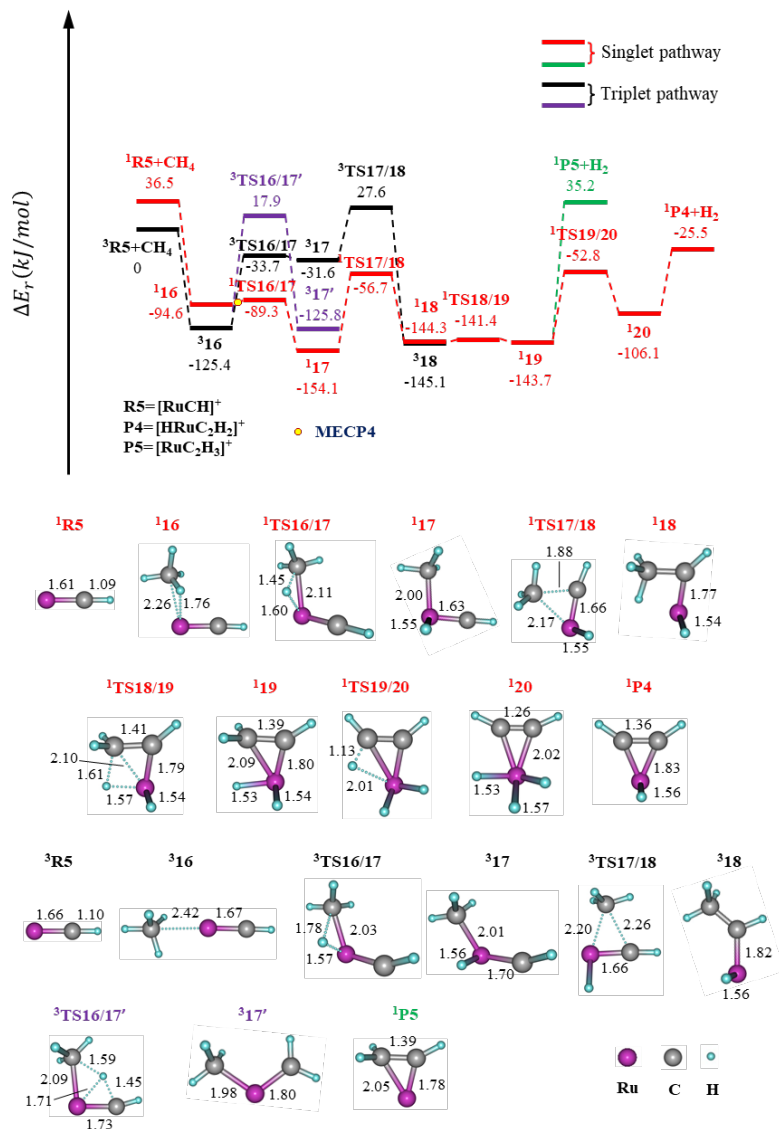
Figure S8 The detailed potential energy profiles of the reaction of [FeCH]$^+$ with CH$_4$.

The reaction processes of [FeCH]$^+$ with CH$_4$ are shown in Figure S8. In contrast to the process of methane activation by [RuC]$^+$ and [OsC]$^+$, the best way to activate the initial H$_3$C-H bond of [FeCH]$^+$ with CH$_4$ is the four-center activation, meaning that FeC unity will be inserted into the H$_3$C-H bond. With the transfer of CH$_3$ moiety (^{3}**22**→^{3}**23**) and the transfer of hydrogen atom (^{3}**23**→^{3}**24**), the intermediate ^{3}**24** is formed, which is similar to the corresponding process for [RuC]$^+$. Next, with one more transfer of hydrogen atom (^{3}**24**→^{3}**25**) and the elimination of molecular hydrogen (^{3}**25**→^{3}**P6** + **H$_2$**), the final product [FeC$_2$H$_3$]$^+$ (^{3}**P6**) is produced. It is worth noting that [FeC$_2$H$_3$]$^+$ (^{3}**P6**) prefers to be the dehydrogenation product of [FeCH]$^+$ with methane rather than [HFeC$_2$H$_2$]$^+$ (^{3}**P7**), which is the contrary to the optimal dehydrogenation product of the reaction of [RuCH]$^+$ and [OsCH]$^+$ with activated methane.
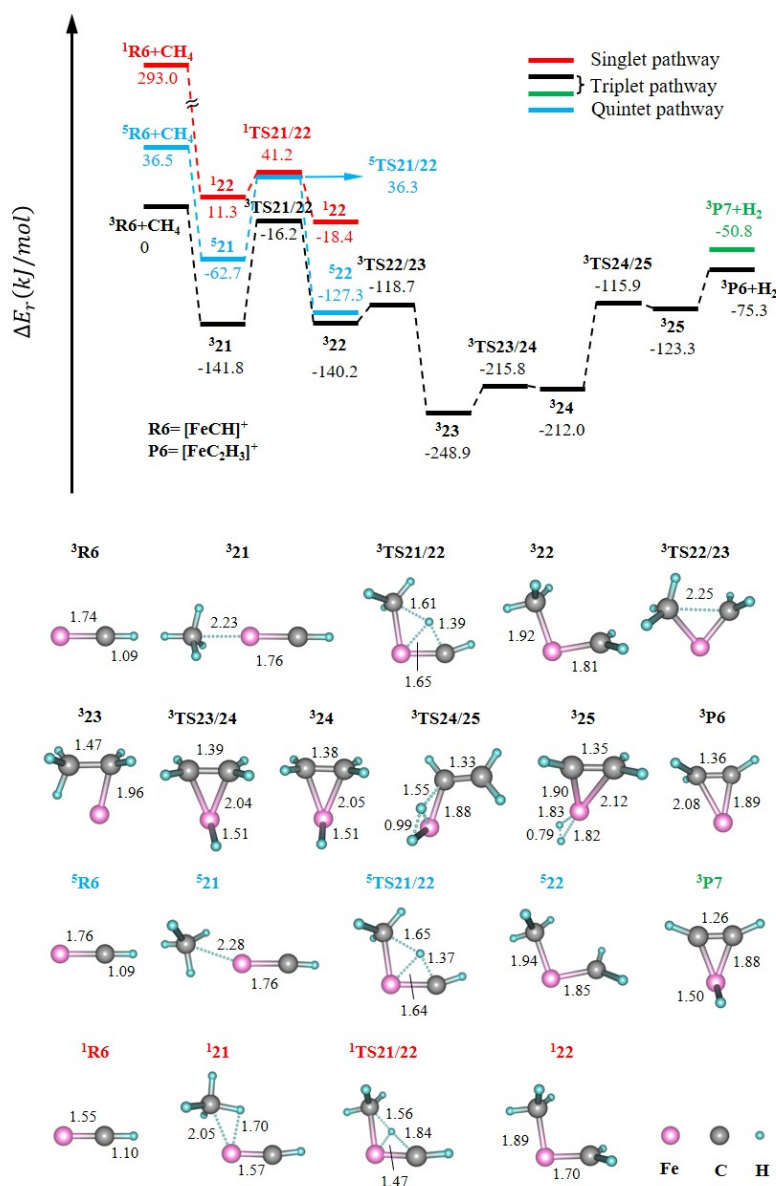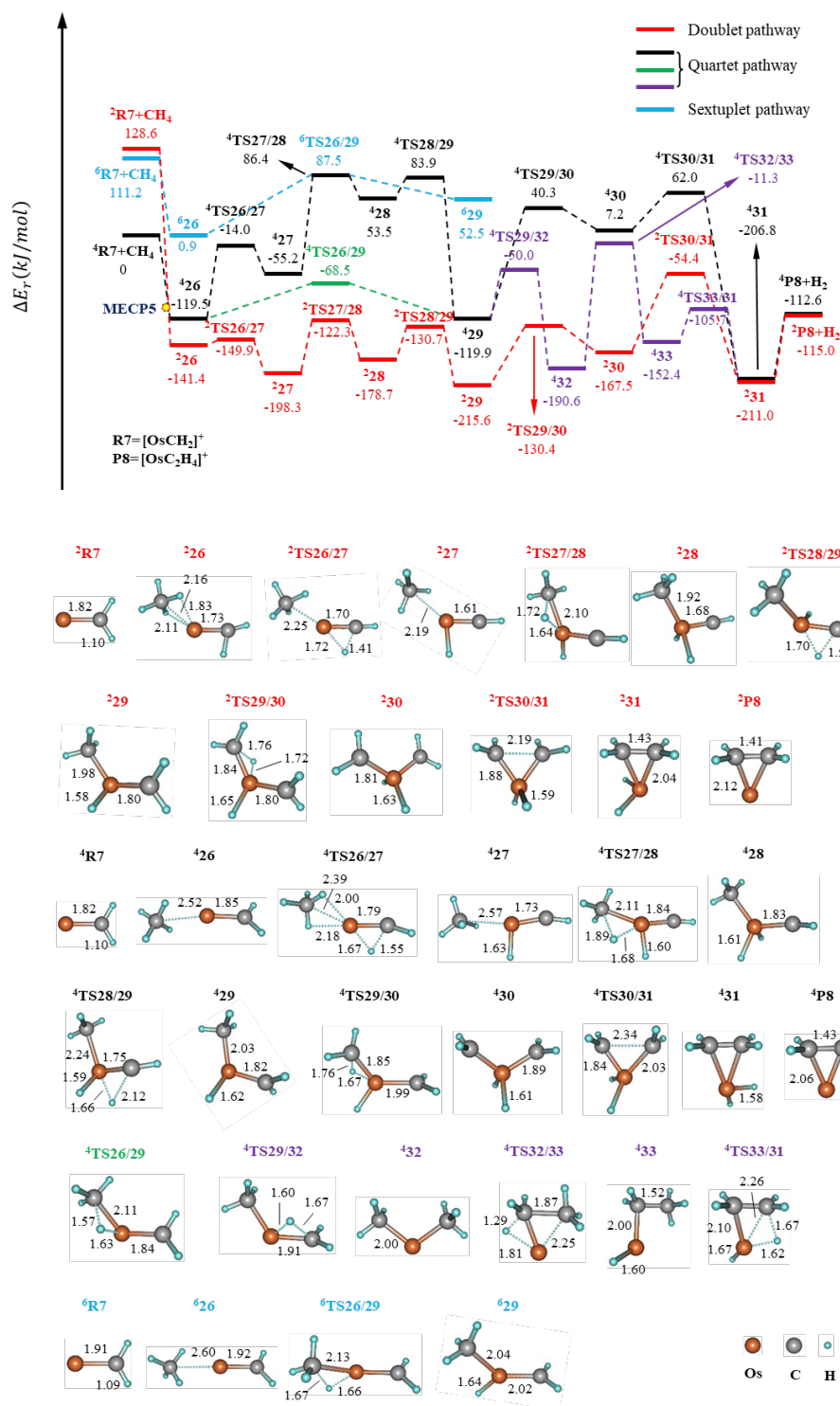
Figure S9 The detailed potential energy profiles of the reaction of $[OsCH_2]^+$ with CH_4

The reaction processes of $[OsCH_2]^+$ with CH_4 are shown in Figure S9. From the pathway, a surface crossing must occur from the quartet state to the doublet state surface in order to form the encounter complex $^2\mathbf{26}$ of the $[OsCH_2]^+/CH_4$ couple. The $[OsCH_2]^+/CH_4$ reaction pathway passes through transformation of hydrogen atom ($^2\mathbf{26} \rightarrow {}^2\mathbf{27}$) to form the intermediate $^2\mathbf{27}$. This implies that it is not the H_3C-H bond activation but the conformational transition of $[OsCH]^+$ that takes place first, which may be due to the agostic interactions.

Consistent with the reaction of $[OsC]^+$ with CH_4, the Os atom is inserted between the HC_3-

H bond (^{2}27→^{2}28). Next, the hydrogen atom transfer from Os to carbide ligand (^{2}28→^{2}29), which is followed by a second hydrogen transfer from the so-formed methyl group to Os (^{2}29→^{2}30). With C-C coupling takes place to afford a η^2-CH$_2$CH$_2$ ligand (^{2}30→^{2}31), molecular hydrogen can be eliminated from the complex (^{2}31→^{2}P8).

It is worth noting that the reaction pathways for the ^{4}[OsCH$_2$]$^+$/ CH$_4$ are diverse. It can directly transfer the H atom from the methane to the carbene ligand (^{4}26→^{4}29) to form intermediate ^{4}29. The subsequent reaction pathway of ^{4}[OsCH$_2$]$^+$/CH$_4$ passes through transformation of hydrogen atom (^{4}29→^{4}32), transformation of CH$_3$ moiety and hydrogen atom (^{4}32→^{4}33) and one more hydrogen atom transformation (^{4}33→^{4}31) to form intermediate ^{4}31. With the cleavage of Os-H bonds, the product ^{4}P7 and H$_2$ are formed. And this process (^{4}29→^{4}32→^{4}33→^{4}31) is unique to ^{4}[OsCH$_2$]$^+$/CH$_4$.
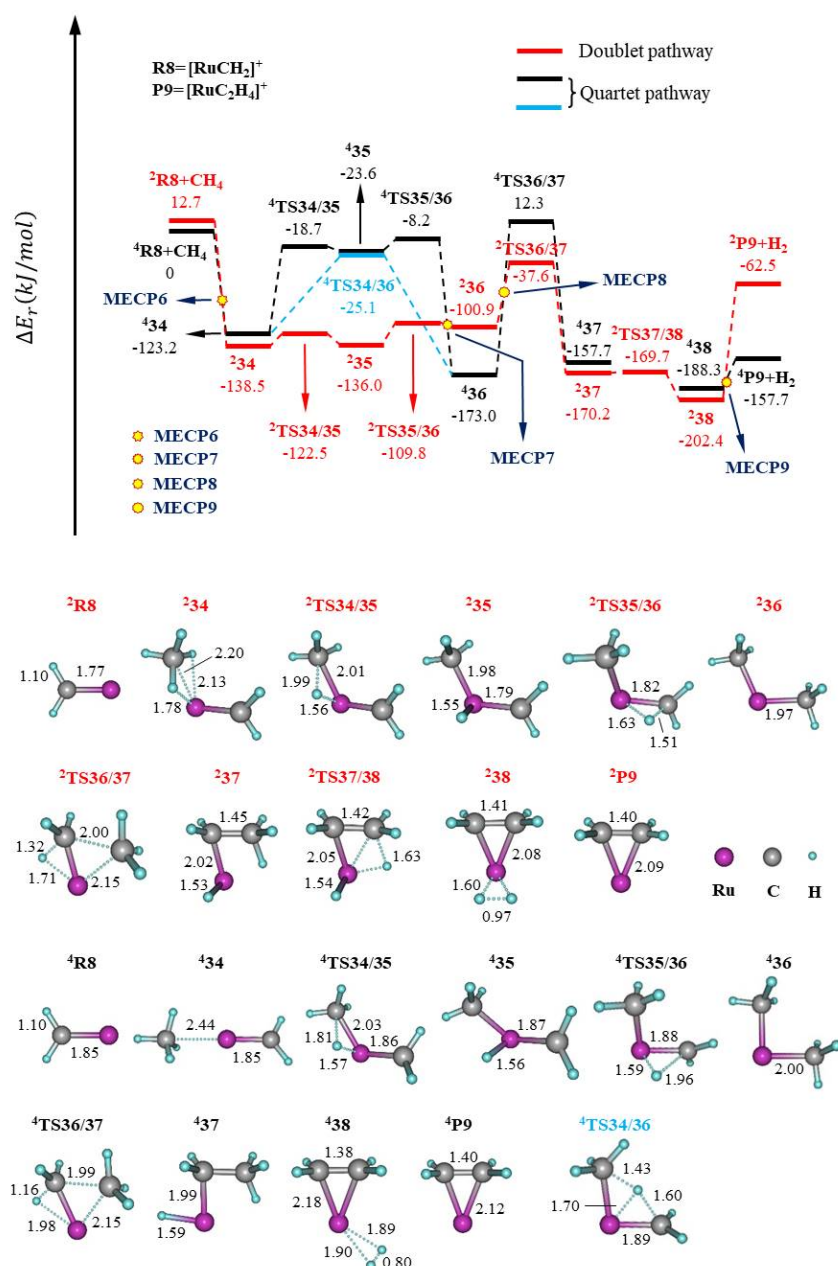
Figure 10 Simplified PES and selected structural information for the reactions of [RuCH$_2$]$^+$ with CH$_4$ as calculated at the DLPNO-CCSD(T)/def2-TZVPP//PBE0-D3(BJ)/def2-TZVP level of theory.

For the reaction of [RuCH$_2$]$^+$ and CH$_4$, the most energetically possible pathways are shown in Figure S10. A surface crossing must occur from the quartet state to the doublet state surface in order to form the encounter complex **^{2}34** of the [RuCH$_2$]$^+$/CH$_4$ couple **(Figure 5)**[12]. Similar to the [OsCH$_2$]$^+$/CH$_4$ couple, the [RuCH$_2$]$^+$/CH$_4$ reaction pathway also pass through transformations of two hydrogen atoms (**^{2}34→^{2}35→^{2}36**) and C-C coupling (**^{2}36→^{2}37**) to form the intermediate **^{2}37**. With one more hydrogen atom transformation (**^{2}37→^{2}38**) and cleavage of Os-H bonds, the the final product (**^{4}[RuC$_2$H$_4$]$^+$** and C$_2$H$_2$) are formed. It's worth noting that dehydrogenation step involves two spin conversions from the quartet state to the doublet state. It should be noted that one PES in the quartet state is more stable, *i.e.* **^{2}36**. Thus, there will be four MECPs (MECP6, MECP7, MECP8 and MECP9) in the pathway, which means four spin conversions between different states. In addition, an energy number -100.9 kJ/mol of **^{2}36** is within the computational error.

The activation of methane by the ^{4}[RuCH$_2$]$^+$ process also has an initial activation process similar to that of [FeCH$_2$]$^+$, *i.e.* the transfer of the hydrogen atom to the C ligand (**^{4}34→ ^{4}TS34/36→^{4}36**). In contrast, the ^{2}[RuCH$_2$]$^+$ does not have a similar activation process, which may be due to the low spin density of Ru.
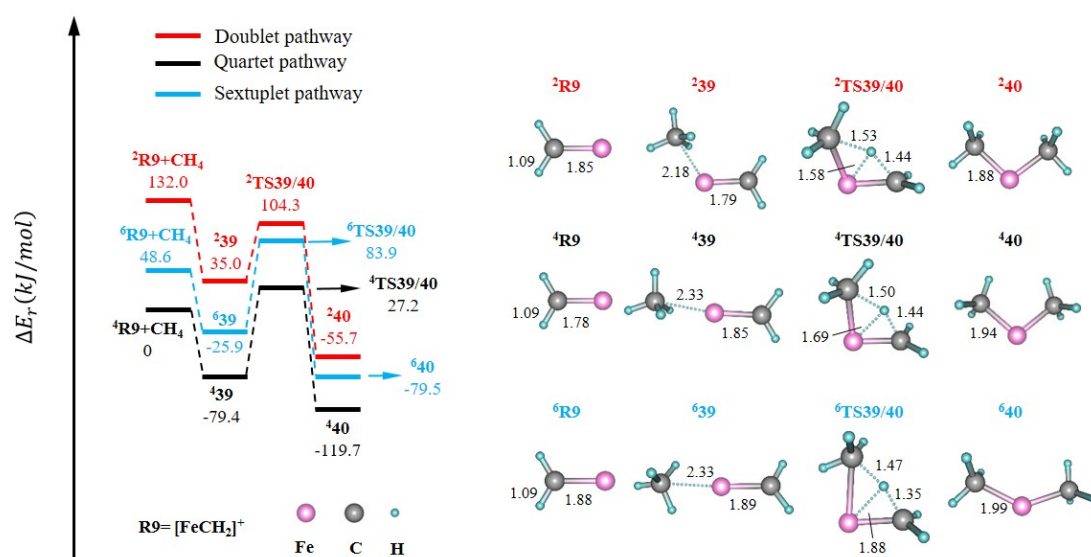
Figure S11 Simplified PES and selected structural information for the reactions of [FeCH$_2$]$^+$ with CH$_4$ as calculated at the DLPNO-CCSD(T)/def2-TZVPP//PBE0-D3(BJ)/def2-TZVP level of theory.

From the pathways in Figure S11, [FeCH$_2$]$^+$ activate the initial H$_3$C-H bond of methane in a similar way to [FeC]$^+$, by transferring H from methane to the C ligand (**39→40**). And [FeCH$_2$]$^+$ cannot cross the energy barrier of the initial H$_3$C-H to activate CH$_4$, in either state.
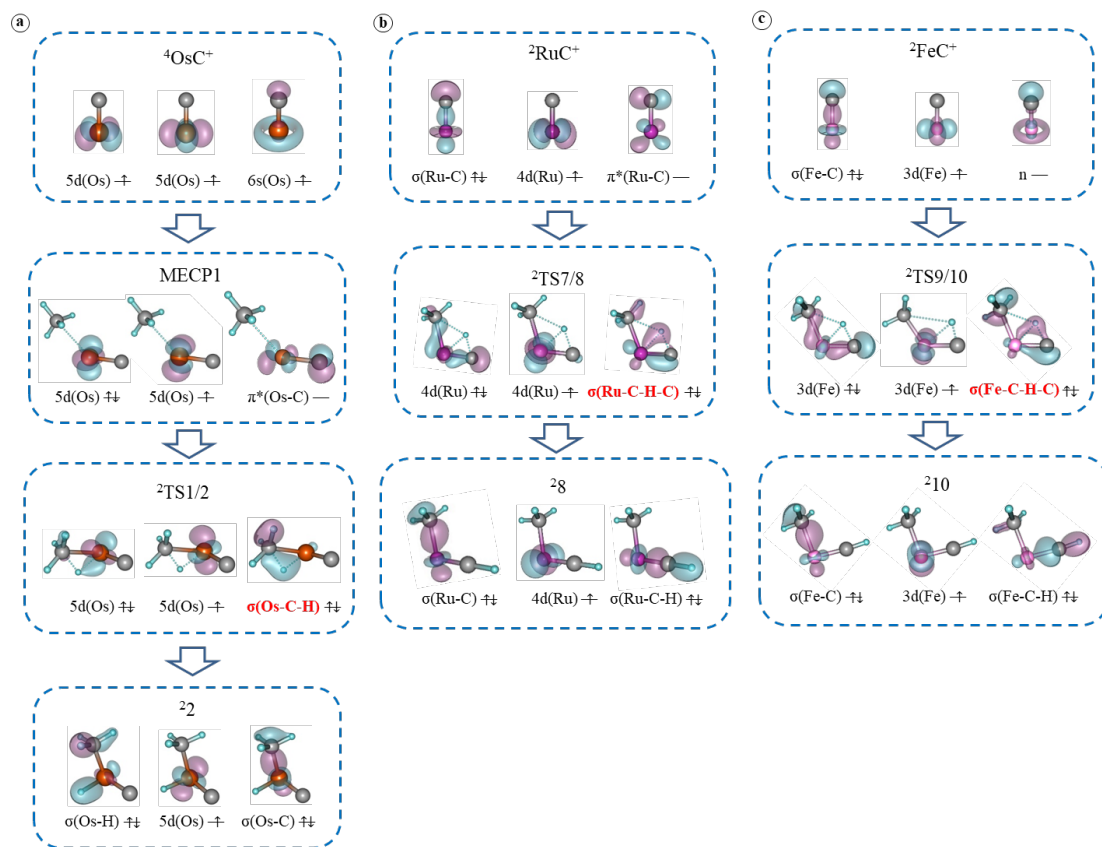
Figure S12 Schematic orbital diagrams represented by natural bond orbitals for the initial H_3C–H bond breaking process for the reaction of (a) $[OsC]^+$, (b) $[RuC]^+$ and (c) $[FeC]^+$ with CH_4.

Schematic representation of the frontier orbitals for $[RuC]^+$, $[FeC]^+$, $[OsCH]^+$, $[RuCH]^+$, $[FeCH]^+$, $[OsCH_2]^+$, $[RuCH_2]^+$ and $[FeCH_2]^+$ are shown in Figure S13-S20, respectively.
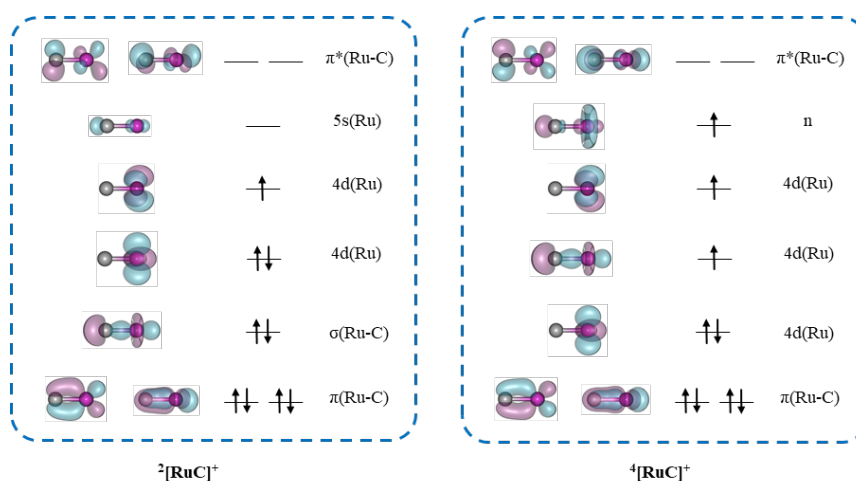
Figure S13 Schematic representation of the frontier orbitals for $[RuC]^+$.
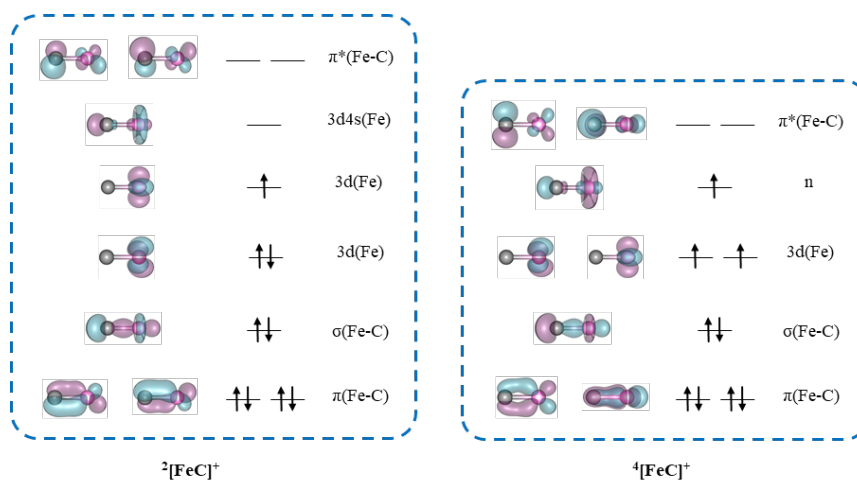
Figure S14 Schematic representation of the frontier orbitals for [FeC]⁺.
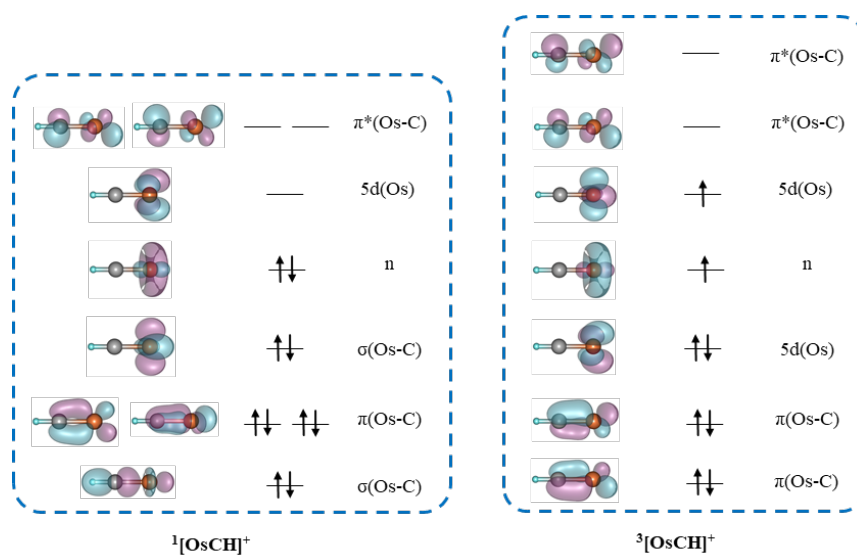
Figure S15 Schematic representation of the frontier orbitals for [OsCH]⁺.
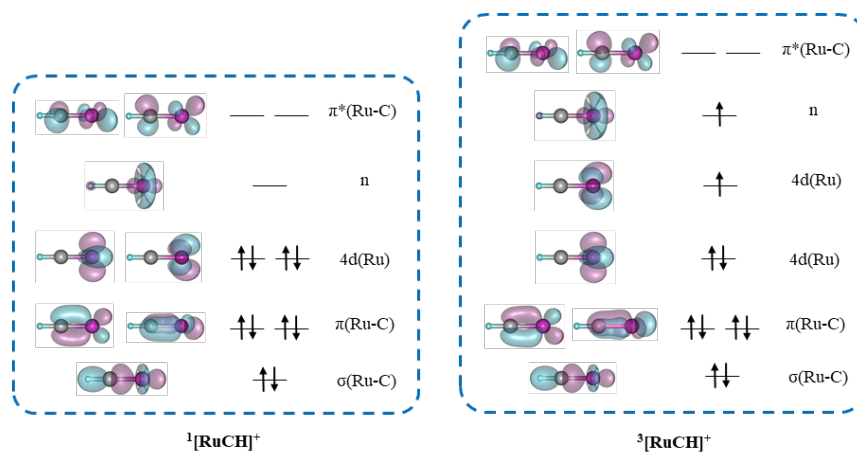
Figure S16 Schematic representation of the frontier orbitals for [RuCH]⁺.
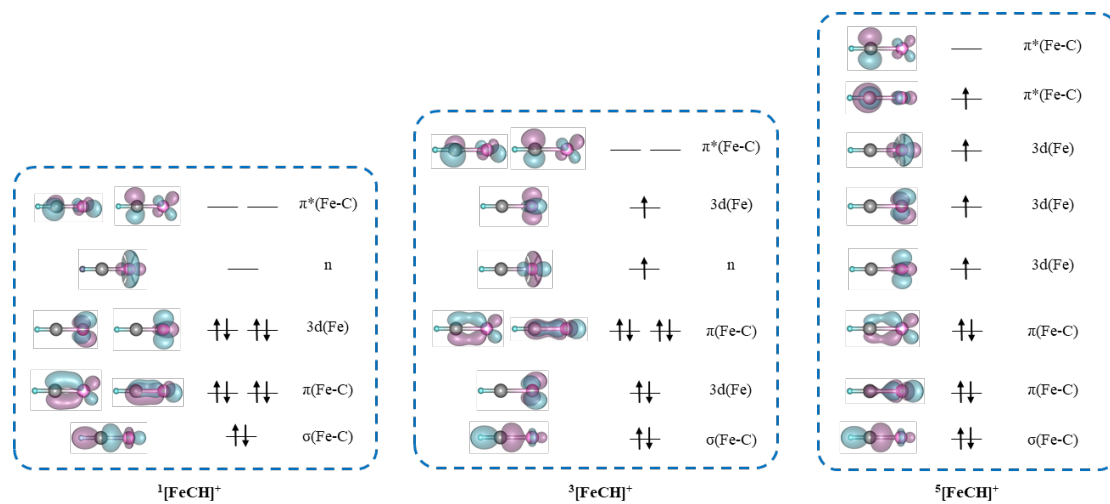
Figure S17 Schematic representation of the frontier orbitals for [FeCH]$^+$.
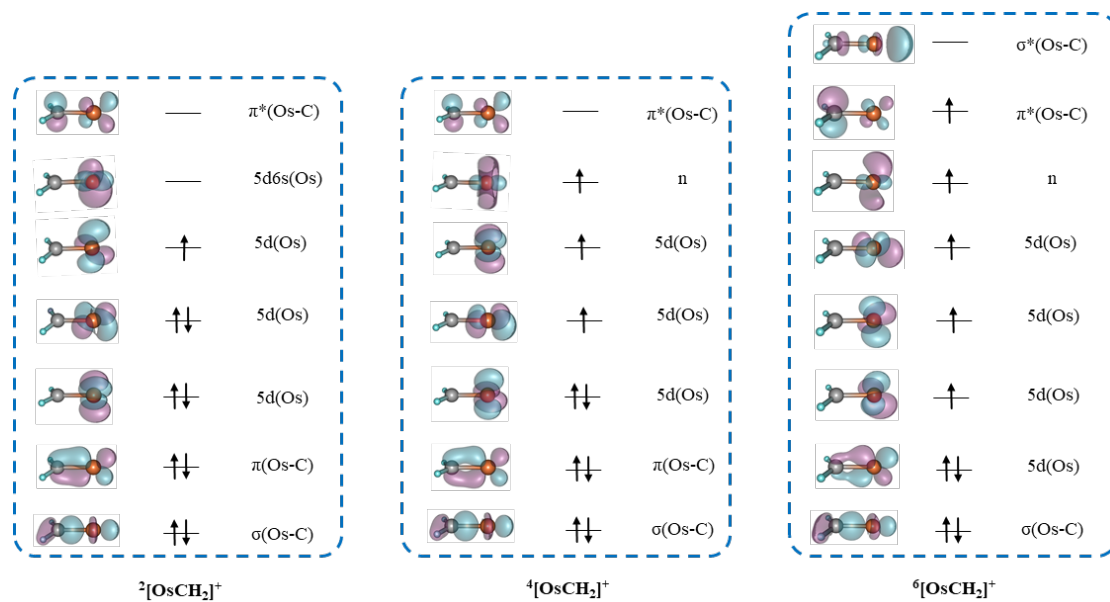
Figure S18 Schematic representation of the frontier orbitals for [OsCH$_2$]$^+$.
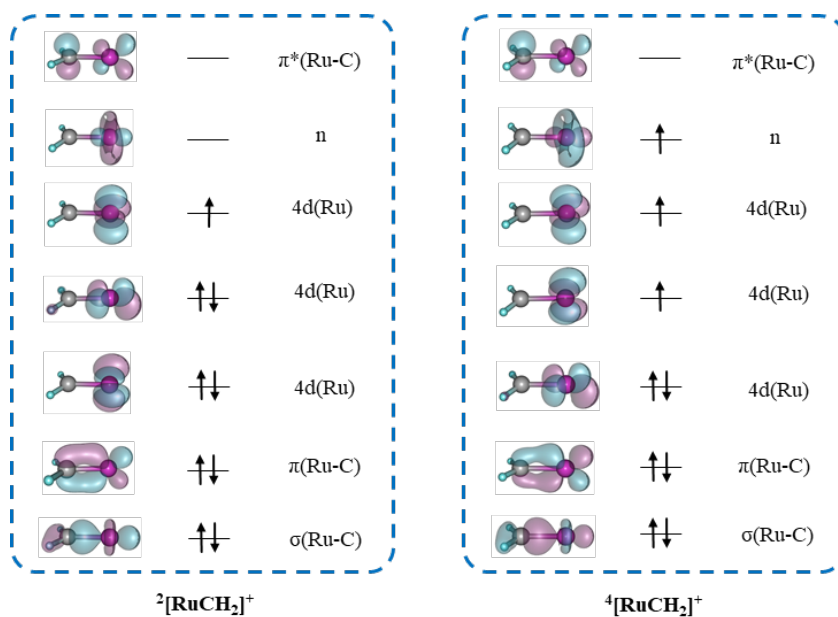
Figure S19 Schematic representation of the frontier orbitals for $[RuCH_2]^+$.
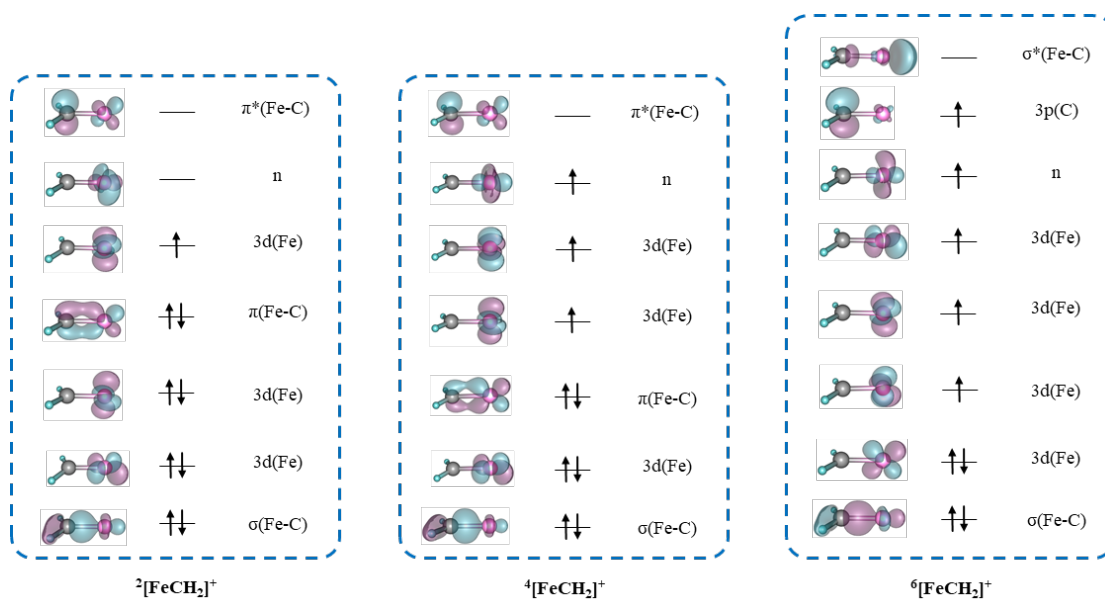
Figure S20 Schematic representation of the frontier orbitals for $[FeCH_2]^+$.

Table S1. The average errors MSE, variances RMSE and the standard deviation of SE of BDE([Os-H]$^+$), BDE ([Os-C]$^+$), BDE ([Os-CH]$^+$), BDE ([Os-CH$_2$]$^+$) and BDE ([Os–CH$_3$]$^+$) for each computational method.

method	BCE(kJ/mol)						analysis		
	[Os-H]$^+$	[Os-C]$^+$	[Os-CH]$^+$	[Os-CH$_2$]$^+$	[Os-CH$_3$]$^+$	average	MSE	RMSE	standard deviation of SE
PBE0-D3(BJ)	-7.678	-18.108	-13.883	-6.725	-29.574	-15.194	249.907	15.808	8.309
revTPSS	-8.254	23.045	16.855	14.741	17.174	12.712	232.585	15.251	10.840
mPW1PBE	-12.474	-31.605	-26.920	-20.459	-45.685	-27.429	730.809	27.033	11.164
B3PW91-D3(BJ)	-2.794	-11.719	-7.255	-1.424	-32.418	-11.122	208.459	14.438	11.245
G96LYP	11.292	35.162	34.420	38.988	14.386	26.849	712.597	26.695	11.586
mPW1PW91	-12.035	-33.804	-29.208	-21.488	-46.479	-28.603	793.772	28.174	11.594
mPW3PBE	-2.859	-7.774	-4.024	-1.161	-32.498	-9.663	190.380	13.798	11.622
TPSSh	-13.725	-12.429	-8.979	-7.370	-39.306	-16.362	337.125	18.361	11.698
X3LYP	2.947	-19.669	-15.342	7.898	-19.764	-8.786	180.648	13.441	11.815
TPSS-D3(BJ)	-5.133	26.103	26.138	21.703	22.394	18.241	393.905	19.847	11.830
B3LYP-D3(BJ)	4.673	-16.229	-12.516	8.964	-22.187	-7.459	169.078	13.003	12.135
B3P86	14.523	7.372	11.329	16.274	-21.605	5.579	187.533	13.694	13.925
B971	4.959	21.157	29.619	46.886	36.699	27.864	815.773	28.562	14.231
BRxp86	7.432	48.748	39.770	24.484	19.952	28.077	835.137	28.899	14.623
mPW1LYP	-2.303	-37.258	-32.919	-3.182	-24.743	-20.081	516.580	22.728	14.719
SOGGA11-X	-29.571	-45.292	-46.768	-5.588	-18.078	-29.059	911.839	30.197	15.804
M11	60.150	62.963	58.900	94.827	90.948	73.558	4719.211	68.697	15.885
B1LYP	-3.580	-44.661	-40.015	-10.062	-32.500	-26.164	794.354	28.184	16.392
BLYP-D3(BJ)	17.762	56.843	52.850	64.098	37.364	45.783	1974.050	44.430	16.515
ωB97X	4.862	-21.042	-5.446	22.428	22.193	4.599	248.598	15.767	16.648
CAM-B3LYP-D3(BJ)	-0.779	-44.816	-33.609	-5.496	0.577	-16.825	528.191	22.982	18.729
BP86-D3(BJ)	27.553	78.789	74.091	67.690	46.817	58.988	3205.027	56.613	19.143

mPWPW91	7.949	61.873	57.504	44.551	29.836	40.343	1678.872	40.974	19.675
mPWPBE	7.460	63.844	59.604	45.482	30.988	41.476	1785.537	42.256	20.553
B2PLYP	-54.705	10.754	-30.949	-29.337	-21.302	-25.108	896.760	29.946	21.112
B2PLYP-D3(BJ)	-53.190	15.135	-26.187	-23.480	-14.876	-20.520	752.772	27.437	21.961
PBEHPBE	9.153	70.898	66.535	53.486	37.168	47.448	2296.592	47.923	22.463
PW91	11.936	75.539	71.279	57.625	40.876	51.451	2653.461	51.512	23.172
ωB97	21.259	-8.365	18.762	54.217	56.395	28.453	1165.633	34.141	24.273
BMK-D3(BJ)	-31.433	-51.375	-38.677	0.032	15.419	-21.207	893.515	29.892	24.950
LC-BLYP	-7.344	-75.147	-64.106	-48.041	-19.649	-42.857	2084.096	45.652	25.771
BPW91	-21.673	50.085	45.885	33.151	20.235	25.537	1098.686	33.146	25.813
M06-HF	50.545	79.217	9.677	71.357	81.426	58.444	3440.954	58.660	26.710
OPBE	-26.213	51.861	48.426	16.103	16.422	21.320	1041.787	32.277	28.207
BPBE-D3(BJ)	-19.846	59.295	56.154	44.380	32.822	34.561	1685.001	41.049	28.767

Table S2. The average errors MSE, variances RMSE and the standard deviation of SE of BDE($[Ru-H]^+$), BDE ($[Ru-C]^+$), BDE ($[Ru-CH]^+$), BDE ($[Ru-CH_2]^+$) and BDE ($[Ru–CH_3]^+$) for each computational method.

| method | BCE(kJ/mol) | | | | | | analysis | | |
	$[Ru-H]^+$	$[Ru-C]^+$	$[Ru-CH]^+$	$[Ru-CH_2]^+$	$[Ru-CH_3]^+$	average	MSE	RMSE	standard deviation of SE
BRxp86	40.889	-52.365	87.003	66.460	55.665	39.530	3249.836	57.007	48.344
mPWPBE	17.211	-60.623	86.078	55.678	43.687	28.406	2731.581	52.265	49.709
PW91	19.316	-51.508	94.824	63.318	50.949	35.380	3103.813	55.712	49.728
mPWPW91	17.107	-63.093	83.479	54.085	42.100	26.736	2656.633	51.543	49.731
BPW91	15.944	-72.114	74.821	46.916	35.018	20.117	2413.367	49.126	49.913
OPBE	19.794	-69.126	83.279	41.051	35.943	22.188	2513.791	50.138	50.242
PBEHPBE	19.286	-53.721	91.337	71.216	49.126	35.449	3180.913	56.400	50.601
BPBE-D3(BJ)	18.932	-62.082	85.852	59.165	48.486	30.070	2905.736	53.905	50.820
BP86-D3(BJ)	31.989	-49.441	95.947	81.779	54.098	42.874	3714.658	60.948	51.180
BLYP-D3(BJ)	16.410	-82.572	61.359	66.940	34.395	19.306	2752.734	52.467	54.134
B2PLYP	66.858	-68.816	63.490	66.790	70.185	39.701	3770.581	61.405	54.300
G96LYP	12.485	-98.813	49.288	48.020	16.562	5.508	2488.233	49.882	54.365
B2PLYP-D3(BJ)	-21.252	-154.042	-21.398	-16.986	-13.028	-45.341	4182.775	64.674	54.438
revTPSS	9.601	-117.191	32.904	23.664	23.469	-5.511	2669.889	51.671	56.334
TPSS-D3(BJ)	10.148	-115.969	38.692	28.343	24.905	-2.776	2745.415	52.397	57.331
B3P86	5.170	-143.441	9.849	6.203	9.160	-22.612	3470.234	58.909	60.440
mPW3PBE	-3.461	-151.085	2.115	-2.200	7.146	-29.497	3816.494	61.778	60.908
B3PW91-D3(BJ)	-2.051	-153.304	0.801	0.270	10.675	-28.722	3936.808	62.744	62.444
TPSSh	-1.601	-162.247	-5.025	-6.320	1.422	-34.754	4398.969	66.325	63.804
PBE0-D3(BJ)	-9.999	-165.555	-12.191	-10.368	6.841	-38.255	4635.222	68.082	64.022
mPW1PBE	-12.851	-177.084	-22.471	-20.684	-3.162	-47.250	5411.114	73.560	65.274
B971	-38.821	-168.771	-8.238	10.120	-4.279	-41.998	5029.865	70.922	65.361

mPW1PW91	-12.982	-179.723	-25.218	-22.330	-4.774	-49.005	5604.388	74.862	65.755
B3LYP-D3(BJ)	-4.120	-173.002	-22.629	-0.373	-9.060	-41.837	5090.171	71.345	66.014
X3LYP	-4.991	-176.933	-26.321	-1.754	-8.418	-43.683	5349.457	73.140	67.165
SOGGA11-X	-29.523	-223.530	-75.977	-38.426	-57.275	-84.946	10227.818	101.133	71.116
mPW1LYP	74.415	-112.873	37.426	69.975	68.020	27.393	4866.978	69.764	71.344
B1LYP	-12.335	-204.947	-54.147	-21.277	-22.399	-63.021	7673.654	87.599	72.365
CAM-B3LYP-D3(BJ)	-11.248	-205.817	-48.510	-18.284	-16.047	-59.981	7572.037	87.017	74.086
ωB97	5.884	-167.185	2.285	32.286	24.449	-20.456	4938.485	70.274	74.214
ωB97X	-38.271	-227.329	-58.563	-34.430	-33.440	-78.407	9812.717	99.059	75.018
M06-HF	-6.366	-180.589	-171.624	-12.888	-138.162	-101.926	13560.399	116.449	76.705
BMK-D3(BJ)	-59.087	-259.975	-62.836	-58.109	-138.056	-115.613	16243.819	127.451	78.270
LC-BLYP	-21.292	-238.486	-71.708	-37.138	-26.312	-78.987	10757.049	103.716	81.667
M11	-28.481	-238.311	-191.953	-37.059	-38.131	-106.787	16212.768	127.329	89.732

Table S3. Polarizability α in Different Clusters as Calculated at the PBE0-D3(BJ)/def2-TZVP Level of Theory.

clusters	spin state	α (a.u.)
OsC$^+$	2	26.5
	4	33.6
OsCH$^+$	1	39.2
	3	34.4
OsCH$_2^+$	2	34.0
	4	37.2
	6	38.1
FeC$^+$	2	20.1
	4	34.9
FeCH$^+$	3	24.9
	5	27.2
FeCH$_2^+$	2	30.2
	4	30.7
	6	31.6
RuC$^+$	2	22.2
	4	37.5
RuCH$^+$	1	24.8
	3	33.1
RuCH$_2^+$	2	28.6
	4	36.5

Table S4. Energy Gap (Activation Process with the Lowest Energy Barrier), Charge and Spin Density of M, Charge and Spin Density of C, Polarizability (α), Dipole Moment and the Ratio of Bond Length of M-C to Atomic Radius of M (M-C/M) in Different Clusters as Calculated at the PBE0-D3(BJ)/def2-TZVP Level of Theory. [a]

clusters	spin state	energy gap (eV)	charge of M	spin density of M	charge of C	spin density of C	α (a.u.)	Dipole moment (a.u.)	M-C/M
OsC^+	2	15.28	0.830	1.406	0.170	-0.406	26.5	0.84	0.47
	4	16.90	0.817	3.191	0.183	-0.191	33.6	0.62	0.47
RuC^+	2	17.29	0.712	1.252	0.288	-0.252	22.2	0.85	0.46
	4	16.97	0.714	3.058	0.286	-0.058	37.5	0.59	0.47
FeC^+	2	16.28	0.930	2.721	0.070	-1.721	20.1	1.05	0.47
	4	16.46	0.864	3.566	0.136	-0.566	34.9	0.91	0.46
$OsCH^+$	1	14.70	0.663		0.094		39.2	0.42	0.42
	3	12.31	0.740	2.267	0.011	-0.291	34.4	0.26	0.42
$RuCH^+$	1	14.13	0.635		0.125		24.8	0.12	0.41
	3	15.03	0.704	2.18	0.071	-0.232	33.1	0.10	0.42
$FeCH^+$	3	15.01	0.876	1.357	-0.052	0.643	24.9	0.28	0.43
	5	15.52	1.162	3.495	-0.348	0.513	27.2	0.68	0.43
$OsCH_2^+$	2	12.51	0.998	1.207	-0.397	-0.215	34.0	0.12	0.47
	4	13.82	0.917	3.277	-0.427	-0.373	37.2	0.37	0.47
$RuCH_2^+$	2	14.54	0.885	1.278	-0.264	-0.286	28.6	0.01	0.46
	4	15.91	0.931	3.256	-0.341	-0.267	36.5	0.08	0.47
$FeCH_2^+$	4	17.19	1.188	3.707	-0.601	-0.732	30.7	0.70	0.47
	6	16.73	1.343	4.004	-0.806	1.031	31.6	1.04	0.48

[a] The dipole moment, M- C /M and spin density of M are the most significantly correlated with the energy gap, with correlation coefficients of 0.66, 0.45 and 0.44 respectively.

The multiple linear regression analysis (see Table S5) shows that the dipole moment, M-C/M and the spin density of M are the three important factors affecting the energy gap (activation process with the lowest energy barrier).

Table S5. The Multiple Linear Regression Analysis of Dipole Moment, M- C /M and Spin Density of M with Energy Gap.[a]

	coefficients		collinearity statistics	
	B	Std. Error	tolerance	VIF
dipole moment	0.505	0.236	0.742	1.348
spin density of M	0.205	0.229	0.828	1.207
M-C/M	0.190	0.258	0.831	1.20

[a]All data have been standardized before linear regression analysis; [b]Linear regression through the origin, $R^2=0.477$ (R^2 measures the proportion of the variability in the dependent variable about the origin explained by regression).
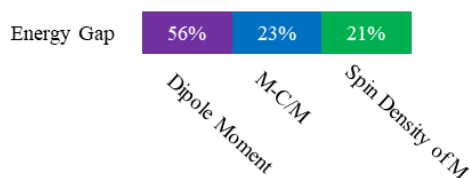
Figure S21 Schematic diagram of the effects of dipole moment, M-C/M and the spin density of M on the energy gap (activation process with the lowest energy barrier)

Table S6. Selected Mulliken Spin Populations for $^4[OsC]^+$.

method	Os	C
PBE0-D3(BJ)	3.299	-0.299
OPBE	3.292	-0.292
BP86	3.197	-0.197
BLYP-D3(BJ)	3.138	-0.138
TPSS-D3(BJ)	3.254	-0.254
TPSSh	3.284	-0.284
B3LYP	3.198	-0.198
CCSD(T)	3.227	-0.227

Table S7. Selected Mulliken Spin Populations for ^{3}[OsCH]$^+$.

method	Os	C	H
PBE0-D3(BJ)	2.330	-0.357	0.026
OPBE	2.268	-0.296	0.028
BP86	2.204	-0.226	0.022
BLYP-D3(BJ)	2.187	-0.207	0.020
TPSS-D3(BJ)	2.246	-0.027	0.022
TPSSh	2.288	-0.312	0.024
B3LYP	2.249	-0.271	0.022
CCSD(T)	2.249	-0.273	0.024

Table S8. Selected Mulliken Spin Populations for ^{4}[OsCH$_2$]$^+$.

method	Os	C
PBE0-D3(BJ)	3.339	-0.429
OPBE	3.239	-0.328
BP86	3.169	-0.258
BLYP-D3(BJ)	3.142	-0.230
TPSS-D3(BJ)	3.233	-0.323
TPSSh	3.289	-0.380
B3LYP	3.239	-0.324
CCSD(T)	3.253	-0.365

Table S9. Selected Mulliken Spin Populations for ^{5}[OsCH$_3$]$^+$.

method	Os	C
PBE0-D3(BJ)	4.033	-0.140
OPBE	3.997	-0.066
BP86	3.962	-0.053
BLYP-D3(BJ)	3.945	-0.046
TPSS-D3(BJ)	3.996	-0.083
TPSSh	4.092	-0.203
B3LYP	4.033	-0.140
CCSD(T)	4.065	-0.141

Table S10. The T1 diagnostic for PESs at the DLPNO-CCSD(T)/def2-TZVPP level of theory.

PESs	T1 diagnostic	PEs	T1 diagnostic	PEs	T1 diagnostic
^{2}R1	0.0215	^{1}R4	0.0154	^{3}17'	0.0269
^{2}1	0.0201	^{1}12	0.0159	^{1}R6	0.0173
^{2}TS1/2	0.0192	^{1}TS12/14	0.0177	^{1}21	0.0185
^{2}2	0.0207	^{1}14	0.0156	^{1}TS21/22	0.0143
^{2}TS2/3	0.0199	^{1}TS14/15	0.0181	^{1}22	0.0191
^{2}3	0.0205	^{1}15	0.0139	^{3}R6	0.0585
^{2}TS3/4	0.0185	^{1}P2	0.0146	^{3}21	0.0520
^{2}4	0.0172	^{1}P3	0.0186	^{3}TS21/22	0.0340
^{2}TS4/5	0.0178	^{3}R4	0.0185	^{3}22	0.0434
^{2}5	0.0185	^{3}11	0.0250	^{3}TS22/23	0.0343
^{2}TS5/6	0.0184	^{3}TS11/12	0.0194	^{3}23	0.0304
^{2}6	0.0167	^{3}12	0.0206	^{3}TS23/24	0.0272
^{2}P1	0.0175	^{3}TS12/13	0.0221	^{3}24	0.0279
^{2}TS2/4	0.0191	^{3}13	0.0236	^{3}TS24/25	0.0265
^{2}TS1/3	0.0181	^{3}TS13/14	0.0232	^{3}25	0.0556
^{4}R1	0.0251	^{3}14	0.0252	^{3}P6	0.0585
^{4}1	0.0263	^{3}TS14/15	0.0207	^{3}P7	0.0252
^{4}TS1/2	0.0241	^{3}15	0.0196	^{5}R6	0.0311
^{4}2	0.0235	^{3}P2	0.0190	^{5}21	0.0295
^{4}6	0.0213	^{3}P3	0.0387	^{5}TS21/22	0.0293
^{4}P1	0.0206	^{3}TS11/12'	0.0200	^{5}22	0.0313
^{4}TS1/3	0.0259	^{3}12'	0.0331	^{2}R7	0.0140
^{2}R2	0.0174	^{1}R5	0.0114	^{2}26	0.0197
^{2}7	0.0214	^{1}16	0.0181	^{2}TS26/27	0.0191
^{2}TS7/8	0.0190	^{1}TS16/17	0.0162	^{2}27	0.0184
^{2}8	0.0178	^{1}17	0.0155	^{2}TS27/28	0.0216
^{4}R2	0.0237	^{1}TS17/18	0.0175	^{2}28	0.0180
^{4}7	0.0269	^{1}18	0.0180	^{2}TS28/29	0.0192
^{4}TS7/8	0.0235	^{1}TS18/19	0.0160	^{2}29	0.0208
48	0.0234	^{1}19	0.0155	^{2}TS29/30	0.0216
^{4}TS7'/8'	0.0248	^{1}TS19/20	0.0190	^{2}30	0.0187
^{4}8'	0.0284	^{1}20	0.0156	^{2}TS30/31	0.0202
^{2}R3	0.0313	^{1}P4	0.0195	^{2}31	0.0189
^{2}9	0.0280	^{1}P5	0.0205	^{2}P8	0.0264
^{2}TS9/10	0.0223	^{3}R5	0.0200	^{4}R7	0.0390
^{2}10	0.0305	^{3}16	0.0213	^{4}26	0.0282
^{4}R3	0.0371	^{3}TS16/17	0.0199	^{4}TS26/27	0.0213
^{4}9	0.0337	^{3}17	0.0201	^{4}27	0.0216
^{4}TS9/10	0.0317	^{3}TS17/18	0.0219	^{4}TS27/28	0.0249
^{4}10	0.0334	^{3}18	0.0279	^{4}28	0.0222
^{4}[TS9/10]'	0.0370	^{3}TS16/17'	0.0195	^{4}TS28/29	0.0245

Table S11. The T1 diagnostic for PESs at the DLPNO-CCSD(T)/def2-TZVPP level of theory.

PESs	T1 diagnostic	PEs	T1 diagnostic
^{4}29	0.0226	^{2}TS37/38	0.0199
^{4}TS29/30	0.0240	^{2}38	0.0194
^{4}30	0.0218	^{2}P9	0.0254
^{4}TS30/31	0.0262	^{4}R8	0.0317
^{4}31	0.0244	^{4}34	0.0294
^{4}P8	0.0221	^{4}TS34/35	0.0246
^{4}TS26/29	0.0232	^{4}35	0.0249
^{4}TS29/32	0.0240	^{4}TS35/36	0.0261
^{4}32	0.0302	^{4}36	0.0250
^{4}TS32/33	0.0230	^{4}TS36/37	0.0254
433	0.0247	^{4}37	0.0247
^{4}TS33/31	0.0246	^{4}38	0.0274
^{6}R7	0.0223	^{2}R9	0.0382
^{6}26	0.0246	^{2}39	0.0311
^{6}TS26/29	0.0257	^{2}TS39/40	0.0303
^{6}29	0.0245	^{2}40	0.0197
^{2}R8	0.0188	^{4}R9	0.0521
^{2}34	0.0222	^{4}39	0.0475
^{2}TS34/35	0.0214	^{4}TS39/40	0.0314
^{2}35	0.0244	^{4}40	0.0299
^{2}TS35/36	0.0228	^{6}R9	0.0308
^{2}36	0.0267	^{6}39	0.0316
^{2}TS36/37	0.0213	^{6}TS39/40	0.0296
^{2}37	0.0203	^{6}40	0.0262

Table S12. The C (C=<S^2> - <S^2>$_{ideal}$) for PESs at the DLPNO-CCSD(T)/def2-TZVPP level of theory.

PESs	C	PEs	C	PEs	C
^{2}R1	0.0141	^{1}R4	0.0000	^{3}17'	0.0083
^{2}1	0.0018	^{1}12	0.0000	^{1}R6	0.0000
^{2}TS1/2	0.0015	^{1}TS12/14	0.0000	^{1}21	0.0000
^{2}2	0.0021	^{1}14	0.0000	^{1}TS21/22	0.0000
^{2}TS2/3	0.0019	^{1}TS14/15	0.0000	^{1}22	0.0000
^{2}3	0.0034	^{1}15	0.0000	^{3}R6	0.2320
^{2}TS3/4	0.0005	^{1}P2	0.0000	^{3}21	0.2157
^{2}4	0.0009	^{1}P3	0.0000	^{3}TS21/22	0.0704
^{2}TS4/5	0.0015	^{3}R4	0.0041	^{3}22	0.1356
^{2}5	0.0024	^{3}11	0.0112	^{3}TS22/23	0.0693
^{2}TS5/6	0.0019	^{3}TS11/12	0.0018	^{3}23	0.0454
^{2}6	0.0008	^{3}12	0.0018	^{3}TS23/24	0.0212
^{2}P1	0.0017	^{3}TS12/13	0.0037	^{3}24	0.0208
^{2}TS2/4	0.0011	^{3}13	0.0047	^{3}TS24/25	0.0150
^{2}TS1/3	0.0009	^{3}TS13/14	0.0055	^{3}25	0.2415
^{4}R1	0.0083	^{3}14	0.0050	^{3}P6	0.2718
^{4}1	0.0064	^{3}TS14/15	0.0014	^{3}P7	0.0181
^{4}TS1/2	0.0048	^{3}15	0.0016	^{5}R6	0.0477
^{4}2	0.0030	^{3}P2	0.0019	^{5}21	0.0466
^{4}6	0.0025	^{3}P3	0.0127	^{5}TS21/22	0.0267
^{4}P1	0.0031	^{3}TS11/12'	0.0026	^{5}22	0.0176
^{4}TS1/3	0.0059	^{3}12'	0.0095	^{2}R7	0.8761
^{2}R2	0.0051	^{1}R5	0.0000	^{2}26	0.0017
^{2}7	0.0028	^{1}16	0.0000	^{2}TS26/27	0.0013
^{2}TS7/8	0.0012	^{1}TS16/17	0.0000	^{2}27	0.0011
^{2}8	0.0014	^{1}17	0.0000	^{2}TS27/28	0.0018
^{4}R2	0.0100	^{1}TS17/18	0.0000	^{2}28	0.0006
^{4}7	0.0082	^{1}18	0.0000	^{2}TS28/29	0.0010
^{4}TS7/8	0.0051	^{1}TS18/19	0.0000	^{2}29	0.0018
48	0.0041	^{1}19	0.0000	^{2}TS29/30	0.0018
^{4}TS7'/8'	0.0046	^{1}TS19/20	0.0000	^{2}30	0.0004
^{4}8'	0.0035	^{1}20	0.0000	^{2}TS30/31	0.0007
^{2}R3	0.0561	^{1}P4	0.0000	^{2}31	0.0009
^{2}9	0.0384	^{1}P5	0.0000	^{2}P8	0.0033
^{2}TS9/10	0.0178	^{3}R5	0.0055	^{4}R7	0.0135
^{2}10	0.0584	^{3}16	0.0052	^{4}26	0.0112
^{4}R3	0.0801	^{3}TS16/17	0.0018	^{4}TS26/27	0.0021
^{4}9	0.0641	^{3}17	0.0018	^{4}27	0.0034
^{4}TS9/10	0.0437	^{3}TS17/18	0.0035	^{4}TS27/28	0.0028
^{4}10	0.0488	^{3}18	0.0064	^{4}28	0.0029
^{4}[TS9/10]'	0.0837	^{3}TS16/17'	0.0024	^{4}TS28/29	0.0036

Table S13. The C (C=$\langle S^2 \rangle - \langle S^2 \rangle_{ideal}$) for PESs at the DLPNO-CCSD(T)/def2-TZVPP level of theory.

PESs	C	PEs	C
^{4}29	0.0014	^{2}TS37/38	0.0013
^{4}TS29/30	0.0023	^{2}38	0.0010
^{4}30	0.0026	^{2}P9	0.0206
^{4}TS30/31	0.0048	^{4}R8	0.0220
^{4}31	0.0031	^{4}34	0.0186
^{4}P8	0.0033	^{4}TS34/35	0.0026
^{4}TS26/29	0.0026	^{4}35	0.0028
^{4}TS29/32	0.0023	^{4}TS35/36	0.0032
^{4}32	0.0040	^{4}36	0.0032
^{4}TS32/33	0.0028	^{4}TS36/37	0.0018
433	0.0031	^{4}37	0.0023
^{4}TS33/31	0.0042	^{4}38	0.0024
^{6}R7	0.0015	^{2}R9	0.1099
^{6}26	0.0011	^{2}39	0.0553
^{6}TS26/29	0.0015	^{2}TS39/40	0.0565
^{6}29	0.0011	^{2}40	1.1865
^{2}R8	0.0050	^{4}R9	0.1698
^{2}34	0.0032	^{4}39	0.1629
^{2}TS34/35	0.0024	^{4}TS39/40	0.0379
^{2}35	0.0025	^{4}40	0.0341
^{2}TS35/36	0.0022	^{6}R9	0.0044
^{2}36	0.0129	^{6}39	0.0033
^{2}TS36/37	0.0005	^{6}TS39/40	0.0028
^{2}37	0.0013	^{6}40	0.0019

Reference

(1) Yu, M.; Ge, X.; Zhou, S. On the Origins of the Mechanistic Variants in the Thermal Reactions of S_x^+ (X = 1-3) with Benzene. *Phys Chem Chem Phys* **2021**, *23*, 17512-17520.

(2) Yu, M.; Ruan, J.; Qian, C.; Chen, X.; Ge, X.; Zhou, S. On the Electronic Origins of the Different Behaviors of S^+ and $S_2^{+/2+}$ in Methane Activation. *ChemistrySelect* **2020**, *5*, 12764-12769.

(3) Frisch, M. J.; Trucks, G. W.; Schlegel, H. B.; Scuseria, G. E.; Robb, M. A.; Cheeseman, J. R.; Scalmani, G.; Barone;, V.; Mennucci, B.; Petersson, G. A.; Nakatsuji, H.; Caricato, M.; Li, X.; Hratchian, H. P.; Izmaylov, A. F.; Bloino, J.; Zheng, G.; Sonnenberg, J. L.; Hada, M.; Ehara, S22 M.; Toyota, K.; Fukuda, R.; Hasegawa, J.; Ishida, M.; Nakajima, T.; Honda, Y.; Kitao, O.; Nakai, H.; Vreven, T.; Montgomery Jr., J. A.; Peralta, J. E.; Ogliaro, F.; Bearpark, M.; Heyd, J. J.; Brothers, E.; Kudin, K. N.; Staroverov, V. N.; Kobayashi, R.; Normand, J.; Raghavachari, K.; Rendell, A.; Burant, J. C.; Iyengar, S. S.; Tomasi, J.; Cossi, M.; Rega, N.; Millam, J. M.; Klene, M.; Knox, J. E.; Cross, J. B.; Bakken, V.; Adamo, C.; Jaramillo, J.; Gomperts, R.; Stratmann, R. E.; Yazyev, O.; Austin, A. J.; Cammi, R.; Pomelli, C.; Ochterski, J. W.; Martin, R. L.; Morokuma, K.; Zakrzewski, V. G.; Voth, G. A.; Salvador, P.; Dannenberg, J. J.; Dapprich, S.; Daniels, A. D.; Farkas, O.; Foresman, J. B.; Ortiz, J. V.; Cioslowski, J.; Fox, D. J. Gaussian 09, Revision A.02; Gaussian Inc., Wallingford, CT; **2009**.

(4) Neese, F. Software Update: The ORCA Program System-Version 5.0. *Wiley Interdiscip. Rev. Comput. Mol. Sci.* **2022**, *12,* e1606.

(5) Schlegel, H. P.; Schlegel, H. B. Using Hessian Updating to Increase the Efficiency of a Hessian Based Predictor-Corrector Reaction Path Following Method. *J. Chem. Theory Comput.* **2005**, *1*, 61-69.

(6) Truhlar, D. G.; Kilpatrick, N. J.; Garrett, B. C. Reaction‐Path Interpolation Models for Variational Transition State Theory. *J. Chem. Phys.* **1983**, *78*, 2438-2442.

(7) Fukui, K. The Path of Chemical Reactions - The IRC Approach. *Acc. Chem. Res.* **1981**, *14*, 363-368.

(8) Reed, A. E.; Curtiss, L. A.; Weinhold, F. Intermolecular Interactions from a Natural Bond Orbital, Donor-Acceptor Viewpoint *Chem. Rev.* **1988**, *88*, 899-926.

(9) Carpenter, J. E.; Weinhold,F. Analysis of the Geometry of the Hydroxymethyl Radical by the "Different Hybrids for Different Spins" Natural Bond Orbital Procedure. *J. Mol. Struc-Theochem* **1988**, *46*, 41-62.

(10) Reed, A. E.; Weinhold, F. Natural Localized Molecular Orbitals. *J. Chem. Phys.* **1985**, *83*, 1736-1740.

(11) Reed, A. E.; Weinstock, R. B.; Weinhold, F. Natural Population Analysis. *J. Chem. Phys.* **1985**, *83*, 735-746.

(12) Reed, A. E.; Weinhold, F. Natural Bond Orbital Analysis of Near-Hartree-Fock Water Dimer. *J. Chem. Phys.* **1983**, *78*, 4066-4073.

(13) Weinhold, J. P.; Weinhold, F. Natural Hybrid Orbitals. *J. Am. Chem. Soc* **1980**, *102*, 7211-7218.

(14) Lu, T.; Chen, F., Multiwfn: A Multifunctional Wavefunction Analyzer. *J Comput Chem* **2012**, *33*, 580-592.